Mechanics of Time-Dependent Materials manuscript No.
(will be inserted by the editor)

Thermoviscoelastic Models for Polyethylene Thin Films

Jun Li · **Kawai Kwok** · **Sergio Pellegrino**

Received: date / Accepted: date

Abstract This paper presents a constitutive thermoviscoelastic model for thin films of linear low-density polyethylene subject to strains up to yielding. The model is based on the free volume theory of nonlinear thermoviscoelasticity, extended to orthotropic membranes. An ingredient of the present approach is that the experimentally inaccessible out-of-plane material properties are determined by fitting the model predictions to the measured non-linear behavior of the film. Creep tests, uniaxial tension tests, and biaxial bubble tests are used to determine the material parameters. The model has been validated experimentally, against data obtained from uniaxial tension tests and biaxial cylindrical tests at a wide range of temperatures and strain rates spanning two orders of magnitude.

Keywords Nonlinear viscoelasticity · Free volume model · Polymer thin film

1 Introduction

The present study was motivated by the need for accurate phenomenological models for thin polyethylene films used in the NASA superpressure balloons. These stratospheric balloons, with a diameter in the range 100-150 m, consist of a polyethylene closed envelope constrained by stiff meridional cords[1][2]; they are operated over

J. Li
Graduate Aerospace Laboratories, California Institute of Technology, Pasadena, CA 91125, USA
E-mail: junlime@gmail.com Present address: Dassault Systemes Simulia Corp., Johnston, RI 02919, USA

K. Kwok
Graduate Aerospace Laboratories, California Institute of Technology, Pasadena, CA 91125, USA
E-mail: kwok@dtu.dk Present address: Department of Energy Conversion and Storage, Technical University of Denmark, Roskilde, Denmark

S. Pellegrino
Graduate Aerospace Laboratories, California Institute of Technology, Pasadena, CA 91125, USA
E-mail: sergiop@caltech.edu

a wide range of temperatures and are subjected to multiple day-night pressurization cycles. The design verification of these balloons requires an accurate material model that captures both time and temperature dependence, to provide accurate estimates of the evolution of stress and strain during a flight.

The film that is the focus of this study is designated as StratoFilm 420. It is a three layer co-extrusion of linear low density polyethylene (LLDPE) with a total thickness of 38 μm. It is produced by Charter NEX Films, Inc. from an extrusion process where the DOWLEX resin (http://www.dow.com/polyethylene/eu/en/prod/dowlex.htm) is extruded from a circular die and simultaneously stretched in the transverse direction to achieve near-balanced properties. An ultraviolet inhibitor (UVI) is added to the resin of the two outer layers, in order to provide long duration protection of the inner layer from exposure to ultraviolet radiation. The center layer is 60% of the total thickness. This film was selected for the NASA superpressure balloons because of its strength and ductile behavior at low temperature. Its glass transition temperature is -95°C and, since the range of operational temperature for stratospheric balloons is above -80°C, the present study covers the behavior of the film in the rubbery state.

The aim of the present study is to develop a constitutive model that captures the nonlinear thermoviscoelastic and anisotropic behavior of LLDPE up to the point where non-recoverable deformation begins. A wide range of constitutive models have been developed for the nonlinear thermoviscoelastic behavior of polymers. Continuum models based on multiple integrals were first proposed but found limited usage due to the complexity of the resulting equations. The first widely adopted single integral formulation was proposed by [3][4] [5], who introduced thermodynamically permissible stress or strain dependent material functions into the linear thermoviscoelastic constitutive equations. [6] [7] [8] developed constitutive models based on the activation energy barriers for polymer networks. [9] developed a thermodynamically consistent formulation for the nonlinear behavior of glassy polymers based on the configurational internal energy. A comprehensive overview of the mathematical aspects of existing models was presented by [10].

StratoFilm was first characterized and modeled on the basis of Schapery's theory [11], including a stress-dependent nonlinear correction. Anisotropy and biaxial loading effects were considered [12] [13], and the biaxial model was then implemented in finite element software that was verified with an experimental study of the time varying strains in a pressurized balloon [14]. These initial models were found to be quite accurate at small strain levels, but the analysis of large-strain regions of a balloon, such as the interfaces between the film and the apex/base fittings or the the film and the meridional cords, required models capable of larger strain predictions.

An alternative approach using the free volume model first proposed by [15] was initiated by [16]. Instead of introducing nonlinear functions tailored to experimentally observed deviations from the linear model predictions, the free volume model postulates a relation between the macroscopic, thermoviscoelastic behavior of the film and its free volume. [16] were able to obtain accurate viscoelastic predictions over the temperature range $-10°\mathrm{C}$ to $0°\mathrm{C}$ in a model that combined Rand's linear viscoelastic model with a free volume formulation.

The present paper extends the previous study by [16] to a much wider range of temperatures and stress states. The paper begins with a focused review, in Section 2,

of linear and nonlinear thermoviscoelasticity. This review provides the foundation for the proposed nonlinear thermoviscoelastic model of StratoFilm. The experimental and numerical procedures to determine the model parameters are described in Sections 3 and 4, respectively. Section 5 presents an extensive validation of the model against experimental results for a range of temperatures, strain rates, and loading conditions that include many cases that were not included in the initial determination of the model parameters. The effects of making different choices for the volumetric coefficient of thermal expansion during the development of the model are specifically discussed. Section 6 concludes the paper.

2 Foundation of Proposed Model

The starting point for the proposed model is the standard theory of linear thermoviscoelasticity, coupled with an expression for the time shift factor that depends on changes in free volume that includes both dilatational and distortional effects.

This section presents a brief summary of the linear theory, formulated in one dimension, and followed by the definition of the free volume and the way it introduces nonlinearity in the time and temperature dependent, large-strain behavior. The remaining parts of the section discuss three additional topics: the limitations of linear viscoelastic models for StratoFilm based on dynamic tests, a linear model for orthotropic thin films, and the thermal expansion of StratoFilm.

2.1 Linear Thermoviscoelasticity

In linear thermoviscoelasticity, the stress-strain relation for uniaxial deformation is expressed in terms of the Boltzmann superposition integral, [17]

$$\varepsilon(t) = \int_0^t D(t-s)\frac{d\sigma}{ds}ds + \int_0^t \alpha\frac{dT}{ds}ds, \tag{1}$$

where ε is the total strain, assumed to be infinitesimally small, σ is the nominal stress, and D is the time-dependent creep compliance. The second term accounts for the thermally induced strain with respect to a reference temperature T_0; T is the temperature and α is the linear coefficient of thermal expansion.

For the analysis of real materials over a wide range of time scales, the creep compliance is often described by means of a series of exponential terms, known as the Prony series [18], where each exponential term effectively represents the variation of the creep compliance over a certain time range. The Prony series representation is given by

$$D(t) = D_0 + \sum_{j=1}^{n} D_j(1 - e^{-t/\tau_j}), \tag{2}$$

where t is time, D_0 is the instantaneous compliance, D_j are the Prony coefficients, and τ_j are the corresponding retardation times.

The rate of creep of a polymer is significantly affected by changes of temperature. Considering the reference temperature T_0; at $T > T_0$ the creep rate is higher;

at $T < T_0$ the creep rate is slower. If all processes contributing to the viscoelasticty of a material are equally accelerated by temperature changes, the material is described as thermorheologically simple [17]. Such materials obey time-temperature superposition, which states that any temperature change corresponds to a shift in time.

Hence the thermoviscoelastic behavior of a thermorheologically simple material across a range of time and temperatures can be described in terms of its behavior at the reference temperature T_0, by introducing a change in the time variable. This modified time variable is known as the reduced time, t', which is defined as

$$t'(T_0) = \frac{t(T)}{a(T)}, \tag{3}$$

where a is a suitable function, known as the shift factor. A widely accepted, empirical expression for the time shift factor of polymers is the Williams-Landel-Ferry (WLF) equation [17],

$$\log a = -\frac{c_1(T-T_0)}{c_2+(T-T_0)}, \tag{4}$$

in which c_1 and c_2 are material parameters.

The creep compliances at two different temperatures are then related by

$$D(t,T) = D\left(\frac{t}{a}, T_0\right). \tag{5}$$

which states that the compliance at temperature T and time t is equal to the compliance at the reference temperature T_0 and reduced time t'. Hence, if a set of creep compliance measurements at different temperatures are available, they can be converted to a single reference temperature. On a log-log plot of compliance versus time, this conversion is equivalent to carrying out horizontal shifts by $\log a(T)$.

By carrying out such a conversion to a single temperature we obtain the compliance master curve, which fully describes the small-strain uniaxial behavior of a thermorheologically simple material.

The above formulation can be extended to non-isothermal conditions by expressing the reduced time as a time integral. Equation 3 is then replaced by

$$t' = \int_0^t \frac{ds}{a(T(s))}. \tag{6}$$

and Eq. 1 can then be expressed in terms of reduced time to account implicitly for temperature variations,

$$\varepsilon(t') = \int_0^{t'} D(t'-s)\frac{d\sigma(s)}{ds}ds + \int_0^t \alpha\frac{dT}{ds}ds. \tag{7}$$

2.2 Nonlinear Thermoviscoelasticity

For finite deformations the formulation in Section 2.1 is not accurate. A single-integral approach to capture the effects of large strains was proposed by Knauss and co-workers [15] [19] [20]. The key additional variable introduced in this model, known as free volume model, is the variation in the intermolecular space within the solid. It is argued that varying this space changes the time scale of molecular chain motions in response to imposed deformation, changing the macroscopic rate of thermoviscoelastic response. As the free volume increases, the molecular chains become more mobile and thus can accommodate any imposed deformation more quickly. Macroscopic volume changes associated with mechanical dilatation, thermal expansion, moisture swelling, etc. are all linked to changes in free volume and hence they influence the time shift factor.

The fractional free volume is defined in terms of the total volume, v_0, of the solid and the free volume, v_f, as

$$f = \frac{v_f}{v_f + v_0} \sim \frac{v_f}{v_0} \tag{8}$$

The time shift factor is assumed to be related to the fractional volume through [21],

$$\log a = \frac{B_d}{2.303}\left(\frac{1}{f} - \frac{1}{f_0}\right), \tag{9}$$

where B_d is a material constant and f_0 is the fractional volume in the reference condition (unstressed, at temperature T_0).

The free-volume model is based on the hypothesis that f can be expressed as

$$f = f_0 + \alpha_v(T - T_0) + \delta_v \cdot \theta, \tag{10}$$

The parameters that appear in Eq. 10 are as follows:

- α_v is the volumetric coefficient of thermal expansion;
- θ is the mechanical dilatation
$$\theta = \sum \varepsilon_k, \tag{11}$$
where ε_k is the diagonal component of the mechanical strain tensor;
- δ_v is a constant that relates changes in mechanical dilatation to changes in free volume.

Combining Eq. 9 and Eq. 10 gives

$$\log\ a = -\frac{B_d}{2.303 f_0}\left(\frac{\alpha_v(T - T_0) + \delta_v \cdot \theta}{f_0 + \alpha_v(T - T_0) + \delta_v \cdot \theta}\right). \tag{12}$$

Equation 12 assumes that nonlinear effects originate only from dilatational effects. However, it was later found that distortional, or shearing, deformation is also a source of nonlinear behavior [22] [23]. Such effects can be included in the model by including in Eq. 12 an additional term, and abandoning the physically based free volume f_0 for two model parameters, f_d, f_s:

$$\log\ a = -\frac{B_d}{2.303 f_d}\left(\frac{\alpha_v(T - T_0) + \delta_v \cdot \theta}{f_d + \alpha_v(T - T_0) + \delta_v \cdot \theta}\right) - \frac{B_s}{2.303 f_s}\left(\frac{\varepsilon_{eff}}{f_s + \varepsilon_{eff}}\right). \tag{13}$$

The present study follows the approach in [22] [23] but represents the shear deformation by means of the effective deviatoric mechanical strain,

$$\varepsilon_{eff} = \sqrt{\frac{2}{3}\left[\left(\varepsilon_1 - \frac{\theta}{3}\right)^2 + \left(\varepsilon_2 - \frac{\theta}{3}\right)^2 + \left(\varepsilon_3 - \frac{\theta}{3}\right)^2 + \kappa\varepsilon_6^2\right]} \tag{14}$$

where ε_6 is the in-plane shear strain component, B_s, f_s, κ are additional, distortional material parameters to be determined experimentally.

The determination of B_d, f_d, B_s, f_s, κ in Eqs. 13-14 requires experiments in which dilatational and distortional effects are separated [23], e.g., confined compression tests and shear tests. However, shear tests are not applicable to thin films, which tend to wrinkle instead of deforming in shear. Therefore, in the present study Eq. 13 was modified to the equivalent, alternative form:

$$\log\ a = -\frac{B}{2.303 f_0}\left(\frac{\alpha_v(T-T_0) + \delta_v \cdot \theta + \delta_s \cdot \varepsilon_{eff}}{f_0 + \alpha_v(T-T_0) + \delta_v \cdot \theta + \delta_s \cdot \varepsilon_{eff}}\right). \tag{15}$$

Here, there is a single parameter, B, instead of B_d, B_s, and the additional parameter δ_s relates changes in effective deviatoric strain to changes in free volume, usually $\delta_s < 1$. An advantage of using this equivalent expression of the time shift is that it is easier to obtain initial estimates of the new parameters, for details see Section 4.4.

It should be noted that, regardless of the kind of problem of interest, the nonlinear models described in this section require knowledge of the full three-dimensional strain state in a material.

Lastly, it should be noted that the coefficient of thermal expansion used in the free volume model, Eq. 10, refers to the total thermal strain from the reference temperature. Hence it is defined as:

$$\alpha_v = \frac{\varepsilon_T}{T - T_0} \tag{16}$$

It is not defined from differential increments in temperature and thermal strain.

2.3 Model for Orthotropic Film

The properties of an orthotropic thin film are defined with respect to the in-plane material axes, 1, 2, and the out-of-plane axis, 3. In the case of blown films such as StratoFilm 420, the material axes are respectively the direction of extrusion, denoted as MD (machine direction), and the orthogonal in-plane direction, denoted as TD (transverse direction).

The model is formulated in terms of the engineering strain $\boldsymbol{\epsilon}$ and nominal stress $\boldsymbol{\sigma}$ tensors. For plane stress the out-of-plane stress is zero and the in-plane shear components are denoted with the subscript 6, hence the constitutive relation in Eq. 7 takes the form

$$\boldsymbol{\epsilon}(t') = \int_0^{t'} \mathbf{D}(t'-s)\dot{\boldsymbol{\sigma}}(s)ds + \int_0^t \boldsymbol{\alpha}\dot{T}(s)ds, \tag{17}$$

where

$$\boldsymbol{\epsilon}(t') = \begin{bmatrix} \varepsilon_1(t') \\ \varepsilon_2(t') \\ \varepsilon_3(t') \\ \varepsilon_6(t') \end{bmatrix} \tag{18}$$

$$\boldsymbol{\sigma}(t') = \begin{bmatrix} \sigma_1(t') \\ \sigma_2(t') \\ 0 \\ \sigma_6(t') \end{bmatrix}. \tag{19}$$

and

$$\boldsymbol{\alpha} = \begin{bmatrix} \alpha_1 \\ \alpha_2 \\ \alpha_3 \\ 0 \end{bmatrix} \tag{20}$$

Note the inclusion of ε_3 in the model. It is needed to compute the mechanical dilatation and distortion, which are needed for the computation of the time shift, Eq. 15.

The creep compliance matrix $\mathbf{D}(t)$ that appears in Eq. 17 is given by

$$\mathbf{D}(t) = \begin{bmatrix} D_{11}(t) & D_{12}(t) & D_{13}(t) & 0 \\ D_{12}(t) & D_{22}(t) & D_{23}(t) & 0 \\ D_{13}(t) & D_{23}(t) & D_{33}(t) & 0 \\ 0 & 0 & 0 & D_{66}(t) \end{bmatrix}. \tag{21}$$

Note that the present model is defined in terms of four strain and stress components, to fully capture the in-plane deformation of the film (3 variables), as well as the out-of-plane deformation needed to determine the mechanical dilatation and distortion (1 variable). Hence, the creep compliance matrix is 4×4, which requires 7 independent compliance functions of which 3 are out-of-plane compliance terms (D_{13}, D_{23} and D_{33}). Note that $D_{33}(t)$ is not needed, as the out-of-plane stress is always zero. This advantage would have been lost if the dual approach, in terms of the relaxation modulus matrix, had been chosen. Also note that each entry in $\mathbf{D}(t)$ is represented by a Prony series of the type defined by Eq. 2.

To summarize, the proposed model describes the nonlinear thermoviscoelastic behavior of an orthotropic thin film by means of Eqs. 2, 6, 15, 11, 14 and 17.

2.4 Complexity of StratoFilm

An initial assessment of the linear properties of StratoFilm was carried out at the NASA Goddard Space Flight Center (GSFC) using a Dynamic Mechanical Analyser (DMA). DMA tests were carried out in both MD and TD, at temperatures from -110°C to 50°C in increments of 10°C, and in the frequency range from 100 Hz to 0.1 Hz for each temperature. From the test data, the storage modulus, E', and the damping coefficient, $\tan\delta$, were obtained for each temperature and frequency [24].

A detailed study of LDPE has shown that it is not thermo-rheologically simple over many decades of time [25], which raised doubts about generating the compliance master curves of StratoFilm by conversion to the time domain of dynamically measured properties. Capodagli and Lakes [25] have used a comparison of master curves for storage and damping moduli in their study. Following this approach, the storage modulus data obtained from the DMA tests was temperature-shifted to form a continuous, smooth curve as shown in Fig. 1 for MD loading. A damping coefficient master curve was then generated assuming the same shifts that had been used for the storage modulus curves and the results are also plotted in Fig. 1.

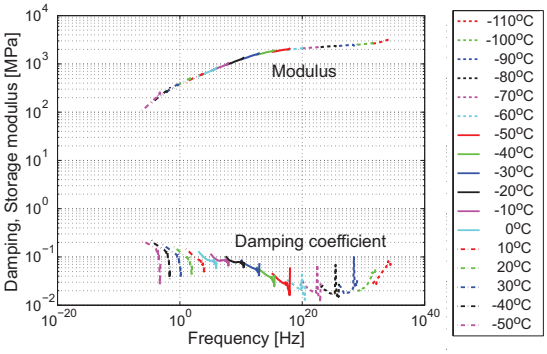

Fig. 1 Master curves of storage modulus and damping coefficient at 20°C in machine direction. The damping coefficient plot is based on the shifts used for the storage modulus.

The figure shows that the damping curves do not form a continuous curve, which indicates that StratoFilm does not obey time-temperature superposition in general. It has been shown that in such cases the time shift factor a becomes dependent on both temperature and frequency [26].

For this reason, as well as unsuccessful attempts to set up a general thermo-viscoelastic model of StratoFilm using material properties based on DMA data, it was decided to use data from creep tests, which are much closer to the balloon operating conditions than DMA tests, to obtain the in-plane creep compliances.

2.5 Thermal Expansion of StratoFilm

Another material property required by the free volume model is the volumetric coefficient of thermal expansion. α_v can be obtained by adding the linear coefficients of thermal expansion (CTE) in three orthogonal directions,

$$\alpha_v \approx \alpha_1 + \alpha_2 + \alpha_3, \tag{22}$$

The in-plane coefficients of StratoFilm 420, α_1 and α_2, were measured by Young [27], see Fig. 2(a), and independently verified in the present study. They are repre-

Table 1 Polynomial representation of in-plane coefficients of thermal expansion.

j	$p_{1,j}$ [K^{-1}]	$p_{2,j}$ [K^{-1}]
0	-2.069691×10^{1}	1.720772×10^{1}
1	1.183351×10^{0}	-1.010550×10^{0}
2	-3.065068×10^{-2}	2.692250×10^{-2}
3	4.755522×10^{-4}	-4.302432×10^{-4}
4	-4.922242×10^{-6}	4.593443×10^{-6}
5	3.580707×10^{-8}	-3.451674×10^{-8}
6	-1.877228×10^{-10}	1.871957×10^{-10}
7	7.146794×10^{-13}	-7.383200×10^{-13}
8	-1.961127×10^{-15}	2.102008×10^{-15}
9	3.783162×10^{-18}	-4.213295×10^{-18}
10	-4.870561×10^{-21}	5.644505×10^{-21}
11	3.757961×10^{-24}	-4.538553×10^{-24}
12	-1.314349×10^{-27}	1.656629×10^{-27}

sented by polynomial functions,

$$\alpha_i = \sum_{j=0}^{N} p_{i,j} T^j, \tag{23}$$

where $p_{i,j}$ are the polynomial coefficients listed in Table 1.

The out-of-plane coefficient, α_3, was measured during the present study. This measurement is challenging due to the small thickness of StratoFilm. Direct measurements were performed with a TA Instruments thermomechanical analyzer (model Q400 0400-0017). The film was cut into 5×5 mm^2 squares and a stack of 20 squares was used to amplify the thermally induced thickness change. The heating rate was set at 2°C/min from -125°C to 55°C.

Choosing an appropriate preload level is crucial, as it is necessary to fully compact the stack before starting the tests, while avoiding significant creep deformation of the test sample. The preload applied to the stack of film layers by the probe of the thermomechanical analyzer was varied between 20 mN and 400 mN. It was found that with a preload of 400 mN the total initial thickness was 0.790 mm, only 4% larger than the thickness of 20 sheets ($0.038 \times 20 = 0.760$ mm). Three test runs were performed for each preload condition and the results were averaged.

The values of α_3 measured for each preload are plotted in Fig. 2(b). The results were found to depend on the preload, the measurements at higher preloads showed broad convergence to

$$\alpha_3 \approx 1 \times 10^{-4} \mathrm{K}^{-1} \tag{24}$$

and this is the value that was chosen for the StratoFilm model. The overall effects on the material model of making alternative choices for α_3 will be discussed in Section 5.3.

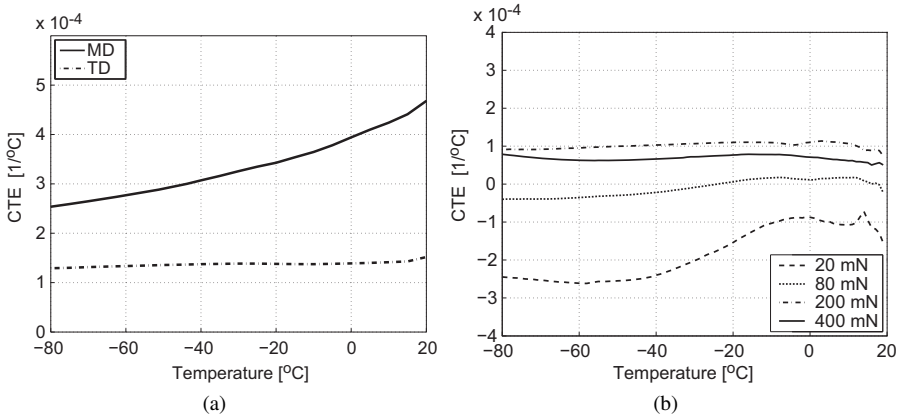

Fig. 2 (a) In-plane and (b) out-of-plane coefficients of thermal expansion. The out-of-plane coefficients were measured under different preloads.

3 Experimental Apparatus and Test Procedures

Three different tests were carried out to characterize the thermomechanical behavior of StratoFilm, including simpler, i.e. uniaxial, stress conditions as well as biaxial stress. Specifically, the following tests were conducted:

- uniaxial tension creep tests to determine the linear in-plane creep compliance master curves;
- uniaxial tension tests at constant strain rate, to activate the nonlinear behavior of the film at larger strains; and
- biaxial bubble tests, to characterize the film behavior under stress conditions that are more representative of the operational conditions in a balloon.

All tests were carried out in an Instron 3119-506 environmental chamber. An Instron 5569 electromechanical materials testing machine was used for the tension tests, and a pressure box placed inside the thermal chamber was used for the bubble tests. Thermocouples were placed close to the top and bottom edges of the test samples to monitor the temperature of the test sample throughout each test.

A three-dimensional digital image correlation (3D-DIC) system [28] was used to measure the biaxial distribution of in-plane strains in the test samples throughout each test. 3D-DIC measure both in-plane and out-of-plane displacements of the film, and hence the correct strains are obtained even in the case that the film is wrinkled. The test samples were lightly sprayed with black paint to provide a random speckle pattern for the 3D-DIC. The images obtained during each test were processed in Vic-3D with a correlation subset of 21×21 pixels and the strain field was computed from an 8-tap B-spline interpolation of the displacement field [29].

The test samples for the uniaxial tests were 10" by 1" strips cut from a single piece of StratoFilm 420 with a JDC Precision Cutter (Thwing-Albert Inc.). The samples were oriented in three directions, MD, TD and 45°, to capture the orthotropy of the

material. The bubble test samples were 10” by 10” squares cut from the same piece of film. The edges of the squares were parallel to the MD and TD.

The creep tests were performed at constant temperatures in the range -70°C to 40°C, at increments of 10°C. A dead load arrangement was used to maintain a constant stress, as the control system in the testing machine was unable to achieve sufficiently uniform conditions and the measurement of small forces was noisy; the test configuration is shown in Figure 3. The load was applied by connecting the bottom end of the sample to a weight, in the range 0.88 N to 9.68 N depending on the temperature, to keep the final strain smaller than 1.5%. This particular strain limit was chosen on the basis of creep tests at NASA Wallops Balloon Research and Development Laboratory, which measured the creep behavior under step increases in the applied stress. A conclusion from these tests was that a longitudinal strain of 1.5% is within the linear creep regime. In the present tests, the top end of the sample was attached to the loading beam of the testing machine and during cooling the beam was held at a lower height, such that the weight was resting on the support block. Thus, the sample remained unstressed throughout the cooling phase. The alignment of the sample grips was carefully checked to minimize any eccentricity in the loading arrangement. Once the test temperature had been reached and it had stabilized within ± 0.3°C, the test started by lifting the loading beam 6 mm at a constant rate of 20 mm/min. The displacement of 6 mm was sufficient to avoid that the weight came into contact with the bottom of the chamber during the test. The sample was then held under constant load for 3 hours. Load transients were monitored by the load cell attached to the loading beam of the testing frame.

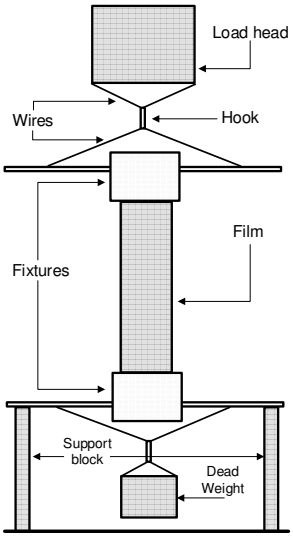

Fig. 3 Small strain creep test configuration.

The imaging rate on the 3D-DIC system was set at 15 sec for these tests. From the load readings it was found that the initial ramp only lasted 5 sec. According to the "ten-times" rule, data recorded after a delay of 50 sec would not show any transient loading effects, which left at least two decades of valid test data at each temperature. Due to the long duration of the small strain creep tests, only two tests were performed at each temperature and the results were averaged in each case.

Figure 4 shows a typical strain field from a creep test in the MD at 20°C. Variations of strains due to boundary effects and experimental noise can be observed. The strain field was averaged over a window near the center of the sample; different sizes of the averaging window were considered but typically the variation of the average strain was less than 3%.

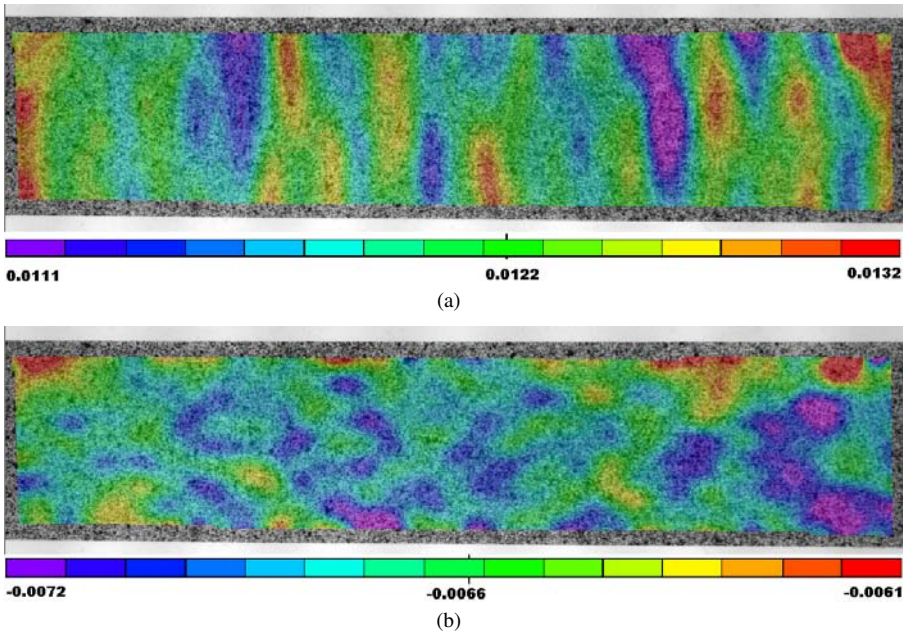

Fig. 4 Strain contour plots from DIC for a small-strain creep test in MD at 20°C: (a) longitudinal strain, (b) transverse strain. The sample width is 1 inch.

The configuration for the uniaxial tests at constant strain rates was similar to the creep tests, but this time the bottom end of the sample was held fixed and the loading beam was continuously moved at a rate such that the test sample was subjected to a nominal strain rate of 0.1% s^{-1}. The tests were continued well beyond the onset of plastic deformation. These tests lasted less than 100 sec and the imaging rate on the 3D-DIC system was set at 0.25 sec to record sufficient data. These tests were carried out at -50°C, -30°C, -10°C and 10°C.

Three samples were tested and averaged for each condition. The nominal stress was calculated from the measured load divided by the initial cross section area of the sample.

The thermal strains were not measured in these tests, as a reference image of the test sample in a slack condition was taken after cooling the sample. Hence, the DIC strain measurements for these tests provided directly the mechanical strain of the sample. Apart from a small difference due to the fact that the initial reference lengths were measured at the test temperature these strain measurements are comparable to those obtained after subtraction of the thermal strains from the total strains (as was the case of the bubble tests, described next). Three specimens were tested under each condition and the plots show little sample variations.

Bubble tests were carried out at -50°C, -30°C, -10°C and 10°C, by clamping StratoFilm samples over an air pressure box with a central hole of diameter 100 mm. The box was connected to an Omega IP610-030 pressure controller to regulate the inlet pressure. The pressure in the box was measured with an Omega DPG409-015G electronic pressure gauge. A National Instruments USB-6221 BNC data acquisition (DAQ) module generated the control signal for the pressure controller and received the signal from the pressure gauge. An Analog Devices AD694JN voltage-to-current (0-10V to 4-20mA) converter was used to convert the voltage signal from the DAQ module to the current signal for the pressure controller. The DAQ module was connected to a personal computer that also processed the deformation measurements from the 3D-DIC and the temperature measurements from the thermocouples, see Fig. 5.

The mechanical strain in the bubble tests was obtained by subtracting the thermal strain, estimated from the second term in Eq. 1, from the total strain measured with DIC.

Because there is a significant mismatch between the thermal expansion coefficients of StratoFilm and the aluminum plate to which the film is clamped, rather large thermal stresses build up during the cooling phase. The nominal stress in the bubble, assumed to be isotropic, was obtained from

$$\overline{\sigma} = \frac{pR}{2h} \tag{25}$$

where h is the initial thickness of the film and R is the mean radius of curvature, obtained from 3D-DIC.

A small overpressure was maintained in the pressure box during cooling to maintain positive curvatures throughout. To avoid initial transient pressure loading effects during cooling, which would complicate the analysis of the measured data, the overpressure was applied 30 min before cooling. Cooling lasted 30 min, then the pressure was increased at a constant rate for 10 min until it reached a specified maximum value, after which the pressure was held constant for 10 min and then it was decreased to zero over 10 min. DIC images were acquired every 5 sec through the whole cooling and testing process; the temperature was also recorded every 5 sec. The window to average the strains and curvatures was located around the apex of the bubble. Typical profiles of pressure and temperature are shown in Fig. 6. Note that the sensitivity

of the pressure controller did not allow us to achieve sudden pressure transitions, or maintain a constant pressure while the temperature was varied.

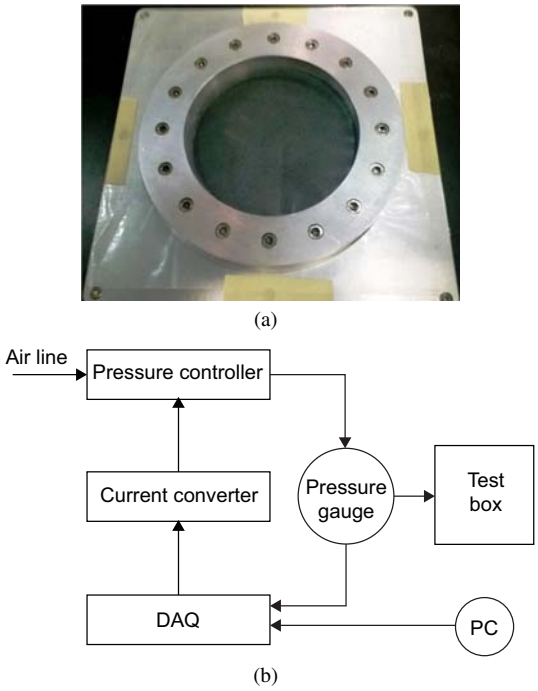

Fig. 5 Bubble test configuration (a) pressure box, (b) schematic of test control.

4 Model Development

The linear orthotropic model outlined in Sections 2.1 and 2.3 consists of the in-plane creep compliance master curves, $D_{11}, D_{22}, D_{12}, D_{66}$. As explained in Section 2.4, these master curves were derived from uniaxial tension creep tests at a series of temperatures.

The nonlinear orthotropic model presented in Sections 2.2 and 2.3 includes the free volume model constants B, f_0, δ_v, δ_s, and the out-of-plane creep compliance master curves D_{13}, D_{23}. Due to the small thickness of StratoFilm direct measurement of the out-of-plane material functions D_{13} and D_{23} would be very challenging. Hence all of the nonlinear model parameters were found by fitting the model predictions to an extensive set of measurement from tests that had activated the nonlinear response of the film.

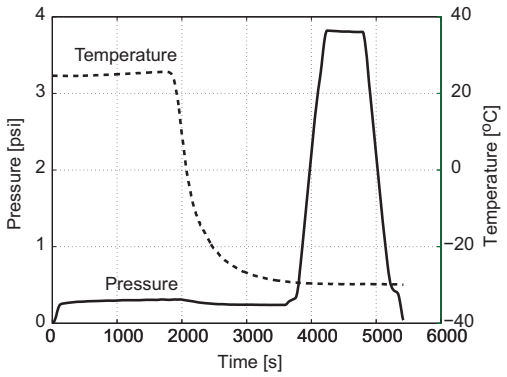

Fig. 6 Profile of pressure and temperature during a bubble test.

4.1 Linear Orthotropic Model

The in-plane creep compliances D_{11} and D_{22} were obtained from the longitudinal strains measured from the creep tests in MD and TD, respectively. D_{12} was obtained by averaging the transverse strains measured during both of these tests. D_{66} was obtained from tests in the 45° direction, which applies a shear stress —in the material coordinate system— in addition to in-plane normal stress components.

The procedure for determining the creep compliance is described next. Let (x,y) denote the axes of the test sample, where the y-axis is aligned with the loading direction; let $(1,2)$ denote the material axes MD and TD, respectively, as already defined in Section 2.3.

First, the nominal x,y stress components were obtained from the applied load:

$$\begin{bmatrix} \sigma_{xx} \\ \sigma_{yy} \\ \sigma_{xy} \end{bmatrix} = \begin{bmatrix} 0 \\ P/wh \\ 0 \end{bmatrix}. \tag{26}$$

where P is the applied load (dead weight) and the $w \cdot h$ is the cross-sectional area of the test sample, measured at the reference temperature.

Second, the mean x,y strain components in the central region of the test sample were obtained from the 3D-DIC measurements, at time intervals of 15 sec for the uniaxial creep tests, 0.25 sec for the constant strain rate tests, and of 5 sec for the bubble tests. The "smooth" function available in Matlab was used to smooth the test data. It uses a moving average filter of 5 data span.

Next, for the tests in the 45° direction, stress and strain transformations were carried out, since in this case the loading axes are rotated by an angle $\theta = 45°$ with respect to the material axes. The transformations are:

$$\begin{bmatrix} \sigma_1 \\ \sigma_2 \\ \sigma_6 \end{bmatrix} = [T] \begin{bmatrix} \sigma_{xx} \\ \sigma_{yy} \\ \sigma_{xy} \end{bmatrix}; \quad \begin{bmatrix} \varepsilon_1 \\ \varepsilon_2 \\ \varepsilon_6 \end{bmatrix} = [R][T][R]^{-1} \begin{bmatrix} \varepsilon_{xx} \\ \varepsilon_{yy} \\ \gamma_{xy} \end{bmatrix}. \tag{27}$$

where $[R] = \text{diag}\{1,1,2\}$ and

$$[T] = \begin{bmatrix} \cos^2\theta & \sin^2\theta & 2\cos\theta\sin\theta \\ \sin^2\theta & \cos^2\theta & -2\cos\theta\sin\theta \\ -\cos\theta\sin\theta & \cos\theta\sin\theta & \cos^2\theta - \sin^2\theta \end{bmatrix}. \quad (28)$$

Finally, the creep compliances were calculated from:

$$D_{11} = \varepsilon_1/\sigma_1 \quad (29)$$

$$D_{12} = \varepsilon_2/\sigma_1 = \varepsilon_1/\sigma_2 \quad (30)$$

$$D_{22} = \varepsilon_2/\sigma_2 \quad (31)$$

$$D_{66} = \varepsilon_6/\sigma_6 \quad (32)$$

The creep compliances derived in this way provided a set of separate curves, each corresponding to one particular temperature. These curves were plotted on a logarithmic time scale and time shifts were applied until each set of curves provided a reasonably continuous and smooth compliance master curve, as shown in Fig. 7. It was found that all four in-plane compliances could be made sufficiently continuous and smooth with the same set of time shifts, which indicates that StratoFilm obeys time-temperature superposition, at least for the creep compliance.

The time shift factors used to generate the master curves have been plotted in Figure 8. They were fitted by Eq. 4, using the Levenberg-Marquardt algorithm to determine the WLF constants c_1 and c_2: $c_1 = 382.2$, $c_2 = 3539.3$ K. It is interesting to compare these results with the universal WLF curve for polymers [30] ($c_1 = 8.86$, $c_2 = 101.6$ K), which is also shown in Fig. 8. It can be seen that at cold temperatures the time shift factors of StratoFilm are much smaller than for a standard polymer.

The final step in the development of the linear model was the computation of the Prony series. Before fitting each experimentally-derived master curve with a Prony series, local waviness was removed by presmoothing the experimental data by means of polynomials, as suggested in [31]. The reason for doing this is that waviness in the master curves for the diagonal coefficients of the creep compliance matrix results in some negative Prony coefficients in Eq. 2. Such negative coefficients indicate an unstable material, which is not physically admissible before the material yields.

For convenience in the implementation of the model, the same values of the retardation times were selected for all four in-plane compliances using one-decade intervals to cover the entire time range of the master curves. This choice has been reported to be adequate for practical applications [32]. The coefficients of the Prony series were obtained by a least squares fit of 37 evenly spaced points selected (2 points per time decade) from each pre-smoothed, experimentally based master curve.

The resulting Prony series fit is quite accurate, see Fig. 9. The coefficients of the Prony series are presented in Table 2.

4.2 Experimental Data for Nonlinear Model

The larger strain uniaxial tension tests at constant strain rate and the bubble tests were used to develop the nonlinear model.

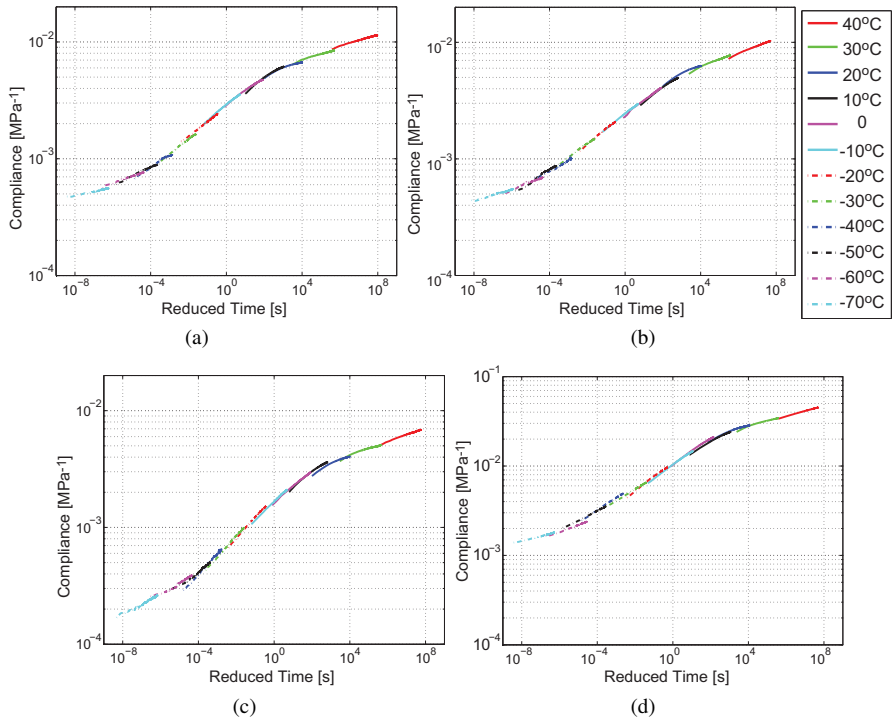

Fig. 7 Compliance master curves at $T_0 = 20°\text{C}$ (a) D_{11}, (b) D_{22}, (c) $-D_{12}$ and (d) D_{66}.

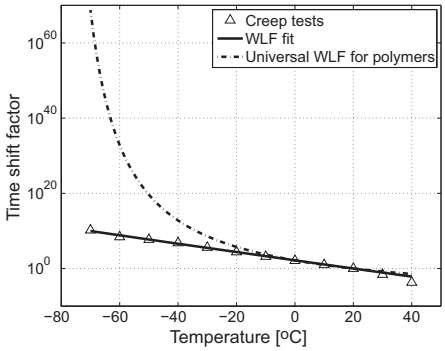

Fig. 8 Comparison of time shift factors from creep tests to universal WLF curve.

Figure 10 shows plots of three sets of longitudinal stress vs. longitudinal strain measurements obtained from uniaxial tension tests at a nominal strain rate of $0.1\%\ \text{s}^{-1}$, at four different temperatures. The nonlinear behavior of StratoFilm at larger strains is evident. Defining yielding as the first point where the stress becomes locally constant in a plot of stress vs. mechanical strain, yielding occurred at a strain of around

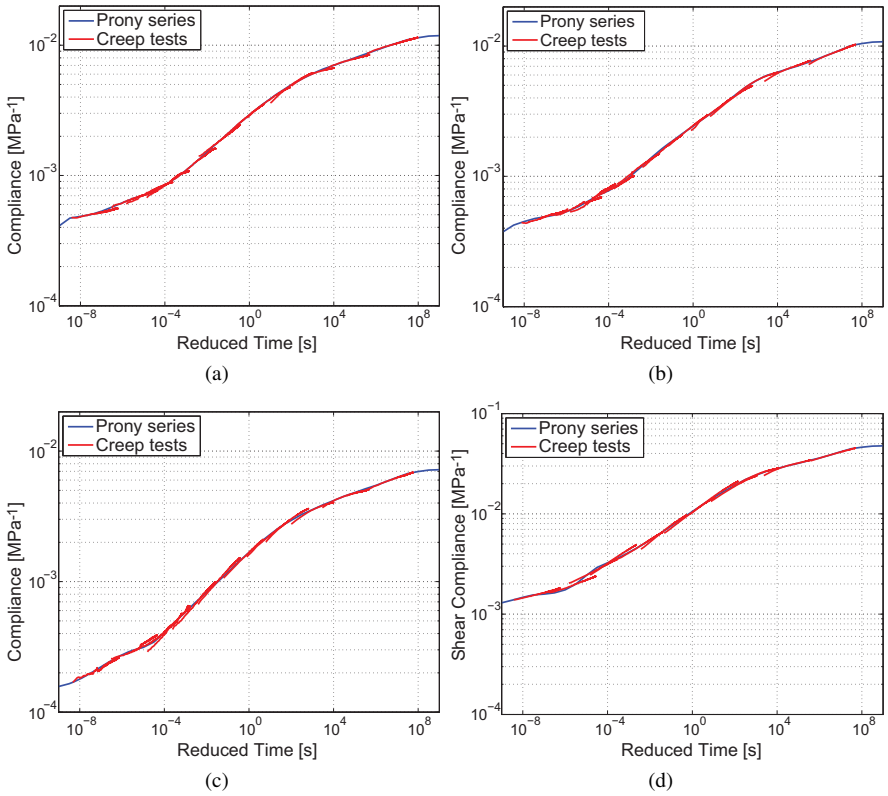

Fig. 9 Prony series fit of compliances (a) D_{11}, (b) D_{22}, (c) $-D_{12}$ and (d) D_{66}.

7% for 10 °C, and at a strain of around 3% for -50°C although the yield stress at this lower temperature was higher.

Figure 11 shows plots of transverse vs. longitudinal strain from the same tests. Overall, these plots are approximately linear, with a slope close to 0.5. This observation indicates that as a first approximation it may be reasonable to assume a time-independent relationship (Poisson's ratio $\nu_{12} \sim 0.5$). A more detailed observation of these plots, however, shows significant orthotropy, nonlinearity and time-dependence.

Figure 12 shows the biaxial total strains (i.e., including both mechanical and thermal strains) and the curvatures measured during a bubble test at -10°C. Note that both sets of plots are almost identical, which indicates that, although the material is orthotropic, the overall structural behavior is close to isotropic. Thus it has been shown that the shape of the bubble is very close to a sphere, and hence that it was reasonable to use Eq. 25 to calculate the stress in the film.

Figure 13 shows plots of nominal stress (computed from Eq. 25) vs. nominal mechanical strain (obtained by subtraction of the thermal strain, computed from Eq. 23, from the total strain obtained form the 3D-DIC measurements), for the full set of bubble tests. As the temperature was decreased between 2000 s and 4000 s, see Fig. 6, the

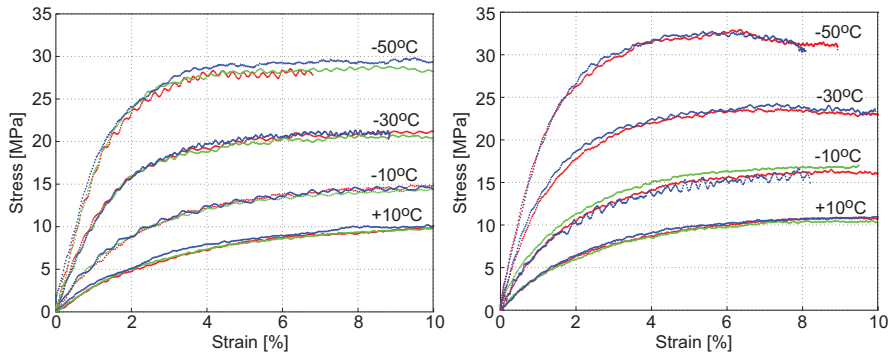

Fig. 10 Longitudinal stress vs. longitudinal strain measured during uniaxial tension tests at a strain rate of 0.1% s^{-1} in (a) MD and (b) TD.

% s

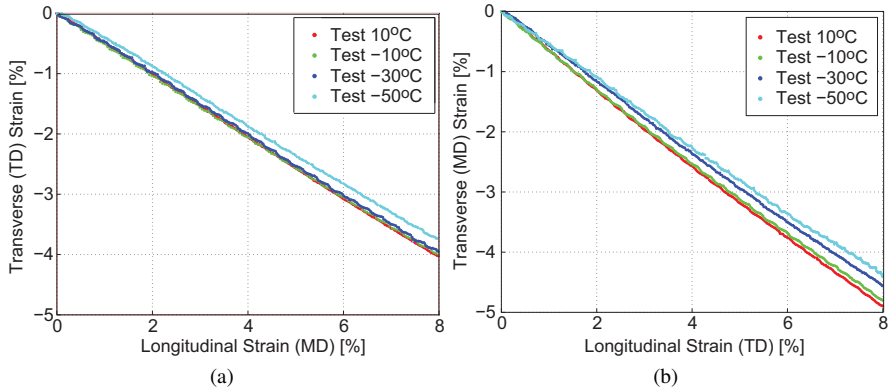

Fig. 11 Transverse strain vs. longitudinal strain measured during uniaxial tension tests at a strain rate of 0.1% s^{-1} in (a) MD and (b) TD.

Table 2 Prony coefficients for D_{11}, D_{22}, D_{12} and D_{66} $[MPa^{-1}]$. In the nonlinear model $D_{12} = -0.5D_{11}$ was assumed.

j	$\tau[s]$	$D_{11,j}$	$D_{22,j}$	$-D_{12,j}$	$D_{66,j}$
0	0	3.0×10^{-4}	3.0×10^{-4}	1.5×10^{-4}	1.2×10^{-3}
1	1×10^{-9}	1.7427×10^{-4}	1.0998×10^{-4}	6.1737×10^{-6}	1.1586×10^{-4}
2	1×10^{-8}	6.5109×10^{-6}	5.8649×10^{-5}	2.7396×10^{-5}	2.4240×10^{-4}
3	1×10^{-7}	6.2843×10^{-5}	2.4143×10^{-5}	5.1691×10^{-5}	3.9937×10^{-6}
4	1×10^{-6}	1.0754×10^{-4}	4.2218×10^{-5}	5.7504×10^{-5}	1.1845×10^{-4}
5	1×10^{-5}	5.8577×10^{-5}	1.5063×10^{-4}	9.2453×10^{-6}	1.0870×10^{-3}
6	1×10^{-4}	1.5508×10^{-4}	9.6093×10^{-5}	1.3158×10^{-4}	5.9741×10^{-4}
7	1×10^{-3}	2.8439×10^{-4}	2.5980×10^{-4}	1.9545×10^{-4}	8.9132×10^{-4}
8	1×10^{-2}	4.5672×10^{-4}	4.4622×10^{-4}	2.4264×10^{-4}	1.5361×10^{-3}
9	1×10^{-1}	6.4614×10^{-4}	4.7934×10^{-4}	3.9097×10^{-4}	2.2114×10^{-3}
10	1×10^{0}	8.6980×10^{-4}	5.9115×10^{-4}	5.3432×10^{-4}	3.3219×10^{-3}
11	1×10^{1}	1.0174×10^{-3}	7.5112×10^{-4}	6.8591×10^{-4}	3.9984×10^{-3}
12	1×10^{2}	1.1201×10^{-3}	1.2374×10^{-3}	6.4146×10^{-4}	5.3721×10^{-3}
13	1×10^{3}	1.0881×10^{-3}	1.2622×10^{-3}	5.7814×10^{-4}	5.0113×10^{-3}
14	1×10^{4}	8.6245×10^{-4}	6.4408×10^{-4}	6.4545×10^{-4}	3.4808×10^{-3}
15	1×10^{5}	1.0593×10^{-3}	8.2460×10^{-4}	6.1626×10^{-4}	3.6546×10^{-3}
16	1×10^{6}	1.1495×10^{-3}	9.4359×10^{-4}	6.1421×10^{-4}	3.8416×10^{-3}
17	1×10^{7}	1.4144×10^{-3}	1.7422×10^{-3}	1.0500×10^{-3}	7.2953×10^{-3}
18	1×10^{8}	9.2623×10^{-4}	7.7978×10^{-4}	5.3076×10^{-4}	3.3653×10^{-3}
19	1×10^{9}	1.3703×10^{-4}	9.7438×10^{-5}	6.8429×10^{-5}	4.2106×10^{-4}

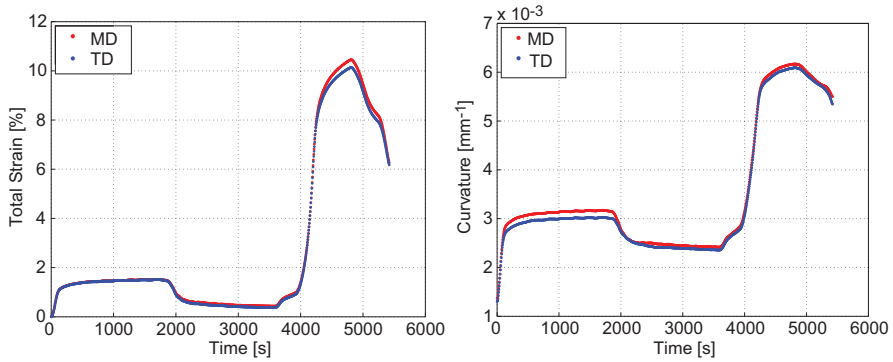

(a) (b)

Fig. 12 Biaxial strains and curvatures vs. time for bubble test at -10 °C: (a) strain and (b) curvature.

(relatively small) mechanical strains in MD and TD are significantly different, due to the thermal anisotropy of StratoFilm. Note that some of the plots in Fig. 13 extend well beyond the point of first yielding for all four tests shown. Also note that during the test at -50 °C condensation behind the window of the environmental chamber caused the stress values, which were obtained from the measured curvatures, to become inaccurate around 4700 s.

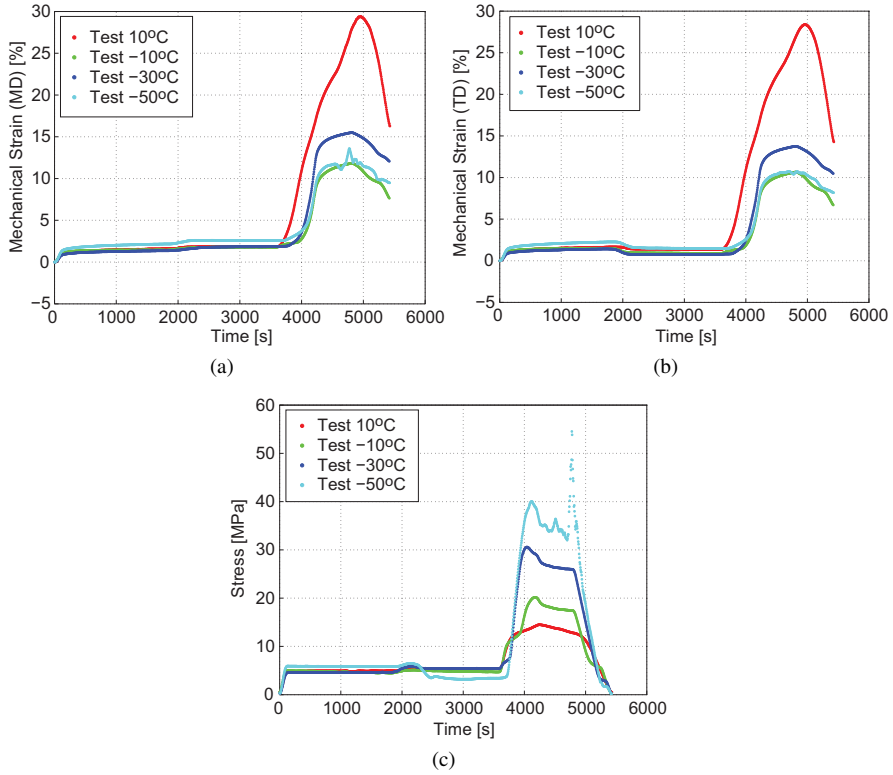

Fig. 13 Variation of strain and stress during bubble tests: (a) MD mechanical strain; (b) TD mechanical strain; (c) mean stress.

4.3 Nonlinear Orthotropic Model

The free volume model parameters B, f_0, δ_v and δ_s in the nonlinear thermoviscoelastic model were determined, together with the out-of-plane creep compliance master curves D_{13}, D_{23}, through a numerical optimization process that maximizes the fit of the model to the experimental results outlined in Section 4.2. In essence, the model parameters were determined by defining an error norm that compares the predictions of models with trial values of the model parameters to data from both uniaxial tension tests and bubble tests. An optimizer was used to search for the set of model parameters that minimize the error norm.

The model implementation was based on a recursive algorithm for linear thermoviscoelastic integrals [33], modified for the free volume model. This approach minimizes the storage and operation count to perform the time integration, as the only history variables required to evaluate the current stress state are the values at the previous time step.

Let the subscripts t' and $t' - \Delta t'$ denote variables at the current (reduced) time step and at the previous time step, respectively. The numerical integration is explained

here for the case of a uniaxial stress state. Following Lai and Bakker [33] Eq. 1 (but including only the mechanical strains) and Eq. 2 can be written in terms of reduced time, in the following form:

$$\varepsilon_{t'} = \tilde{D}_{t'}\sigma_{t'} - f_{t'-\Delta t'}, \tag{33}$$

where

$$\tilde{D}_{t'} = D_0 + \sum_{j=1}^{n} D_j - \sum_{j=1}^{n} D_j \frac{1-e^{-\Delta t'/\tau_j}}{\Delta t'/\tau_j}, \tag{34}$$

$$f_{t'-\Delta t'} = \sum_{j=1}^{n} D_j \left(e^{-\Delta t'/\tau_j} q_{j,t'-\Delta t'} - \frac{1-e^{-\Delta t'/\tau_j}}{\Delta t'/\tau_j}\sigma_{t'-\Delta t'} \right). \tag{35}$$

Here $q_{j,t'}$ is a hereditary integral expressed by

$$q_{j,t'} = e^{-\Delta t'/\tau_j} q_{j,t'-\Delta t'} + (\sigma_{t'} - \sigma_{t'-\Delta t'}) \frac{1-e^{-\Delta t'/\tau_j}}{\Delta t'/\tau_j}. \tag{36}$$

Note that the hereditary integrals $q_{j,t'-\Delta t'}$ and stress $\sigma_{t'-\Delta t'}$ for $f_{t'-\Delta t'}$ have been computed in the previous step. Also note that the reduced time increment $\Delta t'$ in the current step is computed assuming the time shift factor is constant over Δt

$$\Delta t' = \frac{\Delta t}{a_{t'-\Delta t'}}, \tag{37}$$

where the time shift factor $a_{t'-\Delta t'}$ in is determined from the free volume model relationship (Eq. 15):

$$\log\, a_{t'-\Delta t'} = \frac{-B}{2.303 f_0} \left(\frac{\alpha_v (T-T_0) + \delta_v \cdot \theta_{t'-\Delta t'} + \delta_s \cdot \varepsilon_{eff,t'-\Delta t'}}{f_0 + \alpha_v (T-T_0) + \delta_v \cdot \theta_{t'-\Delta t'} + \delta_s \cdot \varepsilon_{eff,t'-\Delta t'}} \right). \tag{38}$$

The mechanical dilatation and distortion have also been determined in the previous step, hence:

$$\theta_{t'-\Delta t'} \cong \varepsilon_{1,t'-\Delta t'} + \varepsilon_{2,t'-\Delta t'} + \varepsilon_{3,t'-\Delta t'} \tag{39}$$

$$\varepsilon_{eff,t'-\Delta t'} \cong \sqrt{\frac{2}{3}\left[\left(\varepsilon_{1,t'-\Delta t'} - \frac{\theta_{t'-\Delta t'}}{3} \right)^2 + \left(\varepsilon_{2,t'-\Delta t'} - \frac{\theta_{t'-\Delta t'}}{3} \right)^2 + \left(\varepsilon_{3,t'-\Delta t'} - \frac{\theta_{t'-\Delta t'}}{3} \right)^2 + \kappa \varepsilon_{6,t'-\Delta t'}^2 \right]}. \tag{40}$$

The multi axial version of Eq. 33 is obtained from Eqs. 17-21

$$\begin{bmatrix} \varepsilon_1 \\ \varepsilon_2 \\ \varepsilon_3 \\ \varepsilon_6 \end{bmatrix}_{t'} = \begin{bmatrix} \tilde{D}_{11} & \tilde{D}_{12} & 0 \\ \tilde{D}_{12} & \tilde{D}_{22} & 0 \\ \tilde{D}_{13} & \tilde{D}_{23} & 0 \\ 0 & 0 & \tilde{D}_{66} \end{bmatrix}_{t'} \cdot \begin{bmatrix} \sigma_1 \\ \sigma_2 \\ \sigma_6 \end{bmatrix}_{t'} - \begin{bmatrix} f_{11}+f_{21} \\ f_{22}+f_{12} \\ f_{13}+f_{23} \\ f_{66} \end{bmatrix}_{t'-\Delta t'} \tag{41}$$

where

$$f_{ij} = \sum_{k=1}^{n} D_{ij,k} \left(e^{-\Delta t'/\tau_k} q_{ij,k} - \frac{1-e^{-\Delta t'/\tau_k}}{\Delta t'/\tau_k}\sigma_i \right) \tag{42}$$

with

$$q_{ij,k} = e^{-\Delta t'/\tau_k} q_{ij,k(t'-\Delta t')} + (\sigma_i - \sigma_{i,t'-\Delta t'}) \frac{1-e^{-\Delta t'/\tau_k}}{\Delta t'/\tau_k} \tag{43}$$

4.4 Model Fitting and Regularization

For any trial set of model parameters, the numerical implementation of the model outlined above can be used to compute the in-plane stress components $\sigma_1, \sigma_2, \sigma_6$ given the in-plane strains $\varepsilon_1, \varepsilon_2, \varepsilon_6$. An issue is that, without direct measurements of thickness changes, θ and δ_v are not distinguishable by the model. Hence, to avoid the non-uniqueness in the determination of θ and δ_v (from D_{13} and D_{23}), we fixed $\delta_v = 1$.

The problem of determining the best set of model parameters, which define the optimization vector $x = [B, f_0, \delta_s, \kappa, D_{13}(t), D_{23}(t)]$, defines the following optimization problem:

$$\min F(x) := \sum_{j \in \mathscr{U}} \omega_1 (\hat{y}_j(x) - y_j)^2 + \sum_{j \in \mathscr{B}} \omega_2 (\hat{y}_j(x) - y_j)^2 \tag{44}$$

where y_j is the jth measured stress data point, in the set of uniaxial tension tests $\mathscr{U}$ or bubble tests $\mathscr{B}$; $\hat{y}_j(x)$ is the jth stress data point predicted by the model, ω_1 and ω_2 are weight factors to bias the optimization more towards the results of the uniaxial tension tests or the bubble tests. Since biaxial stress states are more representative of the balloon operating conditions, $\omega_1 = 1$ and $\omega_2 = 1.5$ were chosen. For convenience $D_{13}(t)$ and $D_{23}(t)$ were expressed by Prony series with the same retardation times as D_{11}, D_{22} and D_{12}, leaving 19 unknown Prony coefficients for each compliance function. Hence, the total number of unknowns in the vector x, to be determined by the optimizer, was 43.

Since there are no known restrictions on the material parameters the problem was treated as an unconstrained optimization problem. Also, since the objective function in Eq. 44 does not lend itself to an analytical expression, it was assumed that the problem is non-convex. Because of the relatively large number of variables, an efficient optimization algorithm known as Covariance Matrix Adaptation Evolution Strategy (CMAES) [34] was selected. The CMAES optimizer is available in Matlab [35].

A two-step optimization process was selected. First, the evolutionary algorithm was used to search the global space. Then a local and efficient simplex optimization algorithm (Matlab's function fminsearch) was used starting from the candidates suggested by CMAES. In fact, it was found that equally good answers could be obtained with "fminsearch" starting from a random initial guess.

A simple initial guess for D_{13} and D_{23} can be made assuming a time-independent Poisson's ratio of 0.5, which gives $D_{13} = -0.5 D_{11}$, and $D_{23} = -0.5 D_{22}$. As for B and f_0, simple initial estimates can be obtained by neglecting the volumetric strain and using Eq. 4 for the time shift factor. The corresponding constants are then related by

$$\frac{B}{2.303 f_0} = c_1, \tag{45}$$

$$\frac{f_0}{\alpha_v} = c_2. \tag{46}$$

where c_1 and c_2 had the values determined in Section 4.1. Hence, the above equations provide an appropriate initial guess for B and f_0. The initial guess of δ_s was chosen as 0.5.

The optimization of the material parameters was carried out for

- sets of 440, 240, 190, 180 uniaxial test data points and 300, 260, 200, 180 uniaxial test data points at temperatures of 10°C, -10°C, -30°C, -50°C, respectively for MD and TD, respectively;
- sets of 766, 825, 806, 810 bubble test data points at temperatures of 10°C, -10°C, -30°C, -50°C.

For the bubble tests the first 360 data points, obtained before cooling, and the data points 361-720 obtained during cooling, i.e. , were weighted less, $\omega_2 = 0.02$, than the data points 721 onwards, $\omega_2 = 0.05$, because the initial set of points corresponded to relatively low pressures.

The initial evaluation of the function F in Eq. 44 gave a value of ~ 600, which was reduced to ~ 100 after 10^5 iterations (set as the limit for the number of iterations). $\delta_s = 0.5$ was used as initial guess. $\delta_v = 1$, fixed for convenience . The initial convergence of error function was fast but then slowed down and after about 10^3 iterations F became almost constant. The results of the optimization were $B = 1.605 \times 10^3$, $f_0 = 1.995$, and $\delta_s = 0.450$.

It was found that a better fit to the experimental data could be obtained, and particularly the transverse stress predicted for the uniaxial tension tests could be kept closer to zero, by using $D_{12} = -0.5D_{11}$, instead of using an independent expression for D_{12} based on its own set of Prony coefficients. This finding is consistent with the observation that the polymer approaches an incompressible rubbery state at larger deformation.

The corresponding Prony series coefficients for D_{13} and D_{23} are listed in Table 3 and these functions are also plotted in Fig. 14.

Figures 15 and 16 compare the uniaxial tension test and the bubble test results to the predictions from the model. Overall, the model fitting captures well the results of both uniaxial tension tests and bubble tests in MD and TD. Note that uniaxial tension tests show somewhat anisotropic material behavior along MD and TD, while for the bubble tests it was assumed that the stress is isotropic, for simplicity.

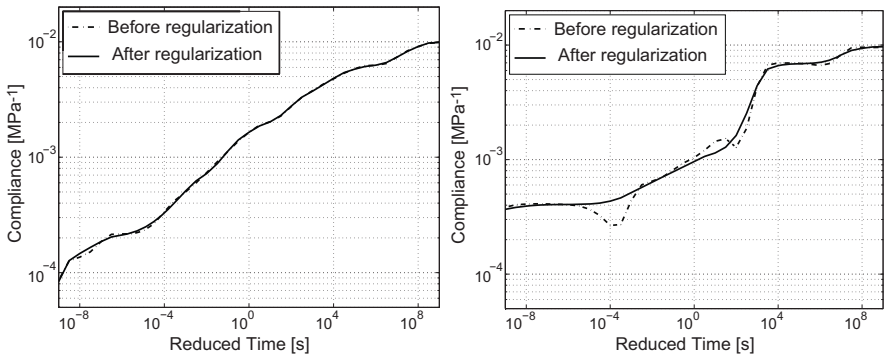

Fig. 14 Creep compliance functions obtained from optimization of material parameters and regularized versions of these functions: (a) D_{13}; (b) d_{23}.

Table 3 Prony series representation of compliances D_{13} and D_{23}.

j	$\tau[s]$	$D_{13,j}[MPa^{-1}]$ (before regularization)	$D_{23,j}[MPa^{-1}]$ (before regularization)	$D_{13,j}[MPa^{-1}]$ (after regularization)	$D_{23,j}[MPa^{-1}]$ (after regularization)
0	0	-8.6222×10^{-6}	-3.4712×10^{-4}	-8.6222×10^{-6}	-3.4712×10^{-4}
1	1×10^{-9}	-1.2140×10^{-4}	-5.6068×10^{-5}	-1.1309×10^{-4}	-2.9719×10^{-5}
2	1×10^{-8}	4.4365×10^{-6}	-9.5061×10^{-6}	-3.1279×10^{-5}	-2.3536×10^{-5}
3	1×10^{-7}	-9.5209×10^{-5}	4.0485×10^{-6}	-4.9324×10^{-5}	-3.6809×10^{-6}
4	1×10^{-6}	1.0630×10^{-5}	-1.0945×10^{-6}	-8.0107×10^{-6}	-1.7406×10^{-6}
5	1×10^{-5}	-3.0625×10^{-6}	3.4154×10^{-5}	-3.3796×10^{-5}	-3.7588×10^{-7}
6	1×10^{-4}	-1.7025×10^{-4}	2.4615×10^{-4}	-9.5429×10^{-5}	-2.5080×10^{-5}
7	1×10^{-3}	-1.3420×10^{-4}	-4.7976×10^{-4}	-2.3780×10^{-4}	-1.0514×10^{-4}
8	1×10^{-2}	-2.7006×10^{-4}	-1.8750×10^{-5}	-1.3354×10^{-4}	-1.3075×10^{-4}
9	1×10^{-1}	-4.2438×10^{-4}	-2.6123×10^{-4}	-5.7668×10^{-4}	-1.4002×10^{-4}
10	1×10^{0}	-6.5437×10^{-4}	-1.2881×10^{-4}	-5.2079×10^{-4}	-2.2724×10^{-4}
11	1×10^{1}	-7.0132×10^{-5}	-8.6797×10^{-4}	-1.5645×10^{-4}	-8.7732×10^{-5}
12	1×10^{2}	-1.1214×10^{-3}	2.0297×10^{-3}	-1.1399×10^{-3}	-1.8575×10^{-5}
13	1×10^{3}	-9.4755×10^{-4}	-7.1174×10^{-3}	-7.6641×10^{-4}	-5.0877×10^{-3}
14	1×10^{4}	-1.0329×10^{-3}	-2.0916×10^{-5}	-1.3667×10^{-3}	-6.0499×10^{-4}
15	1×10^{5}	-1.3129×10^{-3}	-1.2051×10^{-6}	-8.5309×10^{-4}	-3.3549×10^{-6}
16	1×10^{6}	5.2028×10^{-4}	1.1557×10^{-3}	-8.6753×10^{-8}	-5.6042×10^{-5}
17	1×10^{7}	-2.1542×10^{-3}	-3.8565×10^{-3}	-1.6979×10^{-3}	-1.9555×10^{-3}
18	1×10^{8}	-1.7316×10^{-3}	2.1278×10^{-4}	-2.0645×10^{-3}	-8.1855×10^{-4}
19	1×10^{9}	-2.2497×10^{-4}	-1.1180×10^{-4}	-1.4236×10^{-5}	-5.9677×10^{-6}

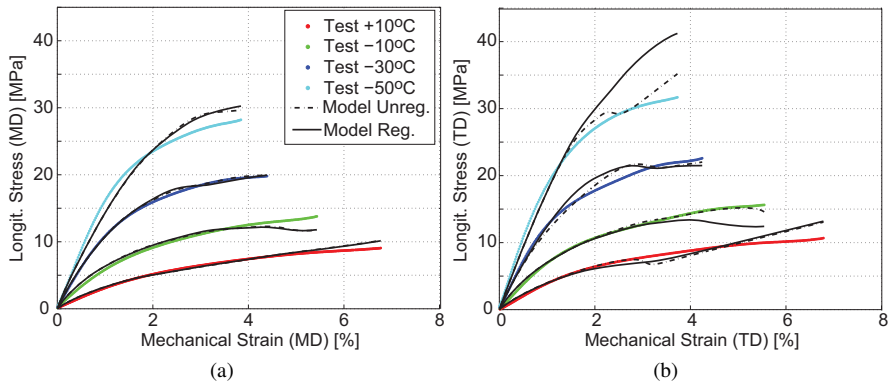

(a) (b)

Fig. 15 Comparison of model predictions to measurements from uniaxial tension tests at strain rate of 0.1% s^{-1} in (a) MD and (b) TD.

The waviness in the model predictions, which can be seen in the plots of these compliance functions in Fig. 14, comes from alternating positive and negative Prony series terms in D_{13} and D_{23}.

The model fitting had been carried out as an unconditional optimization, which allowed sign changes in the parameters. However, the waviness in the model predictions is undesired, as it indicates unstable material behavior. An alternative would

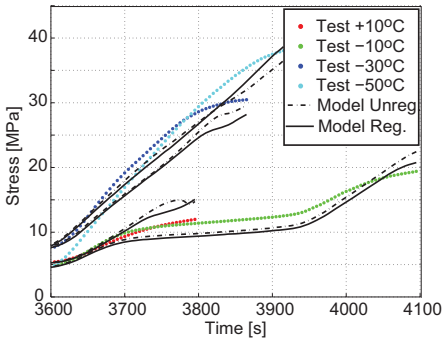

(a)

Fig. 16 Comparison of predictions from two versions of nonlinear model with measurements from bubble tests.

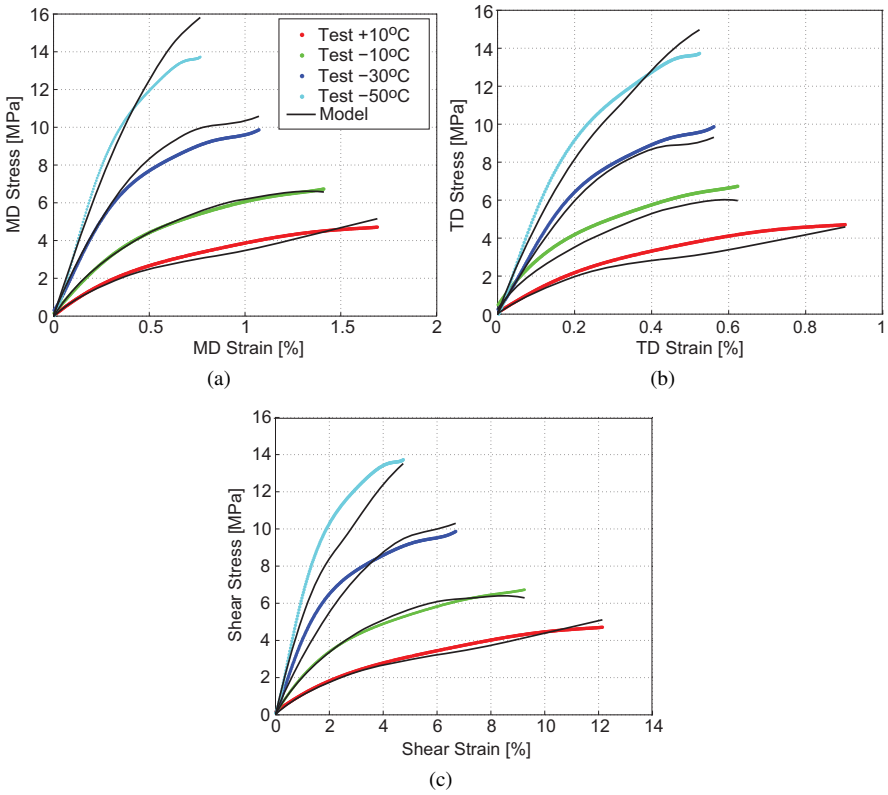

(a) (b)

(c)

Fig. 17 Comparison of regularized nonlinear model with measurements from uniaxial tension tests at 45° from MD, at a strain rate of 0.1% s^{-1}; (a) MD stress vs. MD strain, (b) TD stress vs. TD strain, and (c) shear stress vs. shear strain.

have been the use of a conditional optimizer, but this was found to be computationally rather inefficient.

A more efficient approach is to regularize the Prony series obtained from the unconditional optimization, by subsequently imposing the constraint that the coefficients should all have the same sign. 19 evenly spaced points (one per each time decade) of D_{13} or D_{23} were selected and fitted by Prony series using the constrained least squares fit method (Matlab's function "lsqnonneg"). The functions obtained before and after regularization are plotted in Fig. 14.

The last step in the model fitting is to determine the distortional parameter κ. Recall from Eq. 14 that κ is decoupled from the on-axis uniaxial tests and the bubble tests, because $\varepsilon_6 = 0$ in all of these tests. Therefore, κ was determined by fitting the model independently to the off-axis tests (i.e. uniaxial tension tests at constant strain rate, with the load axis at 45° to MD or TD) after all other model parameters had been determined. Note that, as discussed in Section 4.1, the off-axis uniaxial loading results in non-zero stress components in the material axes $\sigma_1 = \sigma_2 = \sigma_6 = P/(2wh)$. The model implementation employed values of $\varepsilon_1, \varepsilon_2, \varepsilon_6$ from the experiments to calculate $\sigma_1, \sigma_2, \sigma_6$, and iterated over different values of κ to find the best value. The value of κ was obtained by providing 10 random guesses in the range 0 to 1.0 to the "fminsearch" Matlab function. The value that was obtained form this process was $\kappa = 0.24$.

The response of StratoFilm, up to yielding, has been plotted in Fig. 17, to compare the large strain predictions of the model against the experimental results. It can be seen that all model predictions are within 10% of the experiments, including the shear stress versus shear strain comparison, in Fig. 17(c). This last result is remarkable since the shear strains are 6 to 10 times larger than the MD or TD strains, indicating that the shear deformation is dominant.

5 Model Validation and Discussion

The validity of the thermoviscoelastic model developed in the previous sections was assessed by comparing its predictions with experiments involving uniaxial tension tests at different strain rates and also biaxial cylinder tests at different temperatures. None of these test data had been considered during the development of the model, and hence the objective of this validation was to establish the performance of the model when applied to a new situation.

5.1 Validation of Linear Model

The compliance master curves obtained in Section 4.1 were validated against uniaxial tension tests at a constant strain rate of 0.1% s^{-1}. Full results of these tests have already been plotted in Figure 10 and the small strain response (i.e. for longitudinal strains $< 1\%$) was extracted and compared to the model predictions for the smaller strain range. The comparisons are shown in Figs 18-20.

From these comparisons it is found that the linear model provides the correct initial slopes for all of the experiments and at all temperatures. However, the close

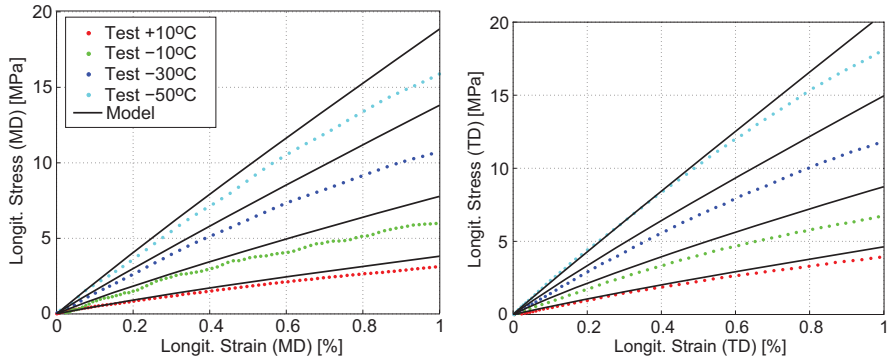

Fig. 18 Validation of linear model for case of longitudinal stress vs. longitudinal strain response in uniaxial tension tests at strain rate 0.1% s^{-1} in (a) MD and (b) TD.

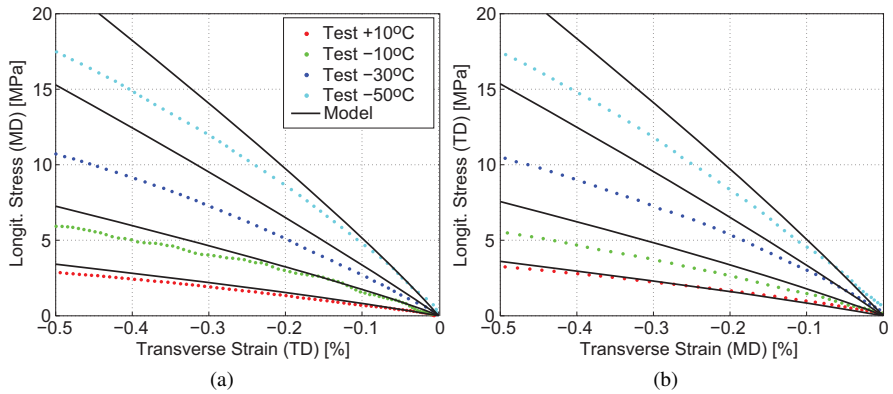

Fig. 19 Validation of linear model for case of longitudinal stress vs. transverse strain response in uniaxial tension tests at strain rate 0.1% s^{-1} in (a) MD and (b) TD.

match between measured and predicted stress values is limited to longitudinal strains of $< 0.4\%$ and transverse strains $< 0.2\%$. For strain magnitudes of 1% the linear model is approximately 30% stiffer. These limits are lower than those used to design small strain creep tests, in Section 3; however it should be noted that the present load condition is different.

The nonlinear model does an excellent job in capturing the strain softening behavior seen in the test data.

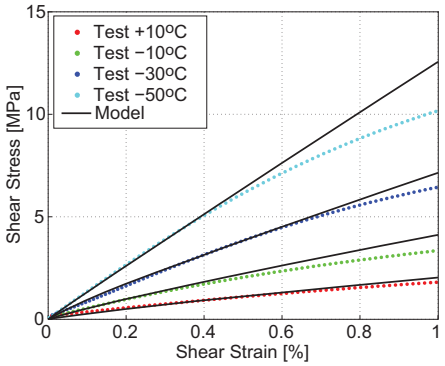

Fig. 20 Validation of linear model for shear stress vs. shear strain response in uniaxial tension tests along 45° from MD at strain rate 0.1% s^{-1}.

5.2 Validation of Nonlinear Model

The nonlinear model with regularized compliance master curves, obtained in Section 4.4, was validated against uniaxial tension tests at constant strain rates that covered two orders of magnitude, as well as cylindrical tests at different temperatures.

The comparison for uniaxial tension included three different strain rates, 0.01% s^{-1}, 0.1% s^{-1}, and 1% s^{-1}, and temperatures of $-20°C$ and $10°C$. The results are presented in Fig. 21; they show the predictions to be very close to the experimental measurements in all cases.

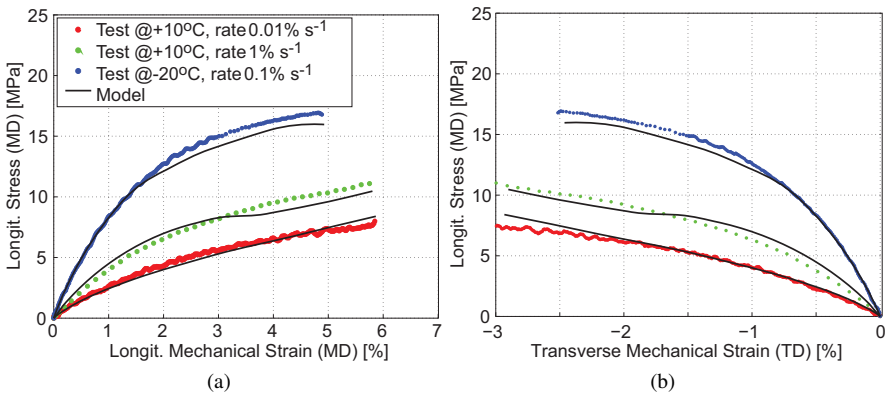

Fig. 21 Validation of nonlinear model in MD by means of uniaxial tension tests at different temperatures and strain rates. Plots of longitudinal stress vs. (a) longitudinal strain and (b) transverse strain.

An additional validation case was provided by a set of experiments done at the NASA Wallops Balloon Research and Development Laboratory. Leyland Young carried out a series of tests on StratoFilm cylinders held inside an environmental tem-

perature. The cylinders were fixed to a horizontal plate at the bottom and to a plate attached to a horizontal beam, through a pulley and weight system that provided an offset for the weight of the plate, at the top. The axial loading on the cylinder was controlled by increasing or decreasing the total weight applied at the end of the pulley, allowing different ratios between the circumferential and longitudinal stress components to be achieved. Each test lasted on the order of 2 mins. Figure 22 shows plots of the mechanical hoop strain vs. the hoop stress computed from the applied pressure, for stress ratios of 2:1 and at two different temperatures. The model predictions corresponding to these tests are also shown in the figure. The agreement is typically within 5%.

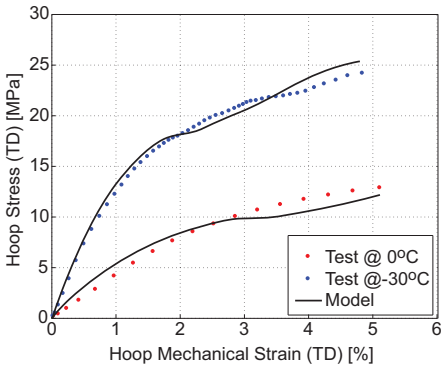

Fig. 22 Validation of nonlinear model for cylinder tests with circumferential/longitudinal stress ratios of 2:1.

5.3 Sensitivity to Volumetric CTE

A distinguishing feature of the proposed model is that the thermal strain and the mechanical strain are combined in the expression for the time shift factor. Hence, the predicted value of the volumetric coefficient of thermal expansion is important to the performance of the model and since, the measurements of α_3 presented in Section 2.5 have left its actual value somewhat uncertain, the sensitivity of the model predictions to the value of α_3 was investigated.

Three values of α_3 were considered:

- model A, with $\alpha_3 = 1 \times 10^{-4}$ as used for the model presented in Section 4;
- model B, with $\alpha_3 = 0$;
- model C, with $\alpha_3 = (\alpha_1 + \alpha_2)/2$.

For each value of α_3, the parameters of the nonlinear thermoviscoelastic model $[B, f_0, \delta_s, \kappa, D_{13}(t), D_{23}(t)]$ were computed following the approach presented in Section 4.4.

A comparison of the predictions from Models A, B, and C, shown in Fig. 23(a) for the specific case of tension tests at a temperature of -20°C and with a strain rate of $0.1\%\ \mathrm{s}^{-1}$ shows practically identical results for the predicted in-plane behavior of the film. However, note that the out-of-plane strains predicted by these models are very different, see Fig. 23(b). Hence, it can be concluded that accurate knowledge of α_3 is not necessary to set up an accurate model of the in-plane behavior. Measurements of the actual out-of-plane response of the film would need to be conducted to determine the actual values of D_{13} and D_{23}.

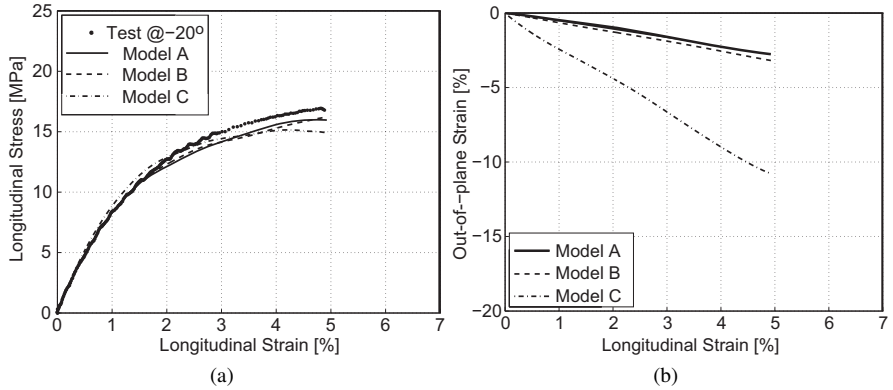

Fig. 23 Comparison between models with different values of α_3, for uniaxial tension tests of (a) longitudinal stress versus longitudinal strain and (b) out-of-plane strain vs. longitudinal strain at T=-20°C strain rate $0.1\%\ \mathrm{s}^{-1}$ in MD.

6 Conclusion

A nonlinear orthotropic thermoviscoelastic model for the large-strain constitutive behavior of the LLDPE film StratoFilm 420 has been developed and validated in this paper. The key feature of the model is that the dependence of the material on time, temperature and strain is captured by a time shift factor that accounts for both dilatational and distortional deformations, assumed to be related to the free volume of the material. The in-plane behavior of the film is characterized by the in-plane compliance functions $D_{11}, D_{22}, D_{12}, D_{66}$, expressed in terms of Prony series with different coefficients but equal retardation times. These functions are obtained from small-strain creep tests that generate master curves (based on the assumption that it is acceptable to superpose time and temperature effects). The out-of-plane behavior of the film, which would be difficult to characterize experimentally in a direct way, is obtained by numerically matching the predictions of the nonlinear model to experimental measurements obtained from specially devised test configurations that induce significant nonlinear material behavior. Hence, the parameters of the nonlinear model, B, f_0, δ_s, κ and the out-of-plane compliances D_{13}, D_{23} are obtained from a two-step

optimization scheme that combines an evolutionary algorithm with a simplex optimization. The out-of-plane compliances presented in this paper were regularized by requiring that there should be no sign changes in the coefficients of each Prony series, to remove excessive oscillation in the model predictions.

Nominal stress and engineering strain definitions were used throughout this study, for both experimental data and model implementation. In principle, the model can be developed in terms of finite strains, however the approach presented in this paper is particularly convenient as the effects of thickness changes in the current configuration on the stress and strain measures, which would further complicate the process of determining the model parameters, are avoided.

A mechanically (but not thermally) isotropic version of the model has also been developed, although not presented here. Finding a smaller set of parameters that avoid spurious oscillations is easier in this case, but the overall accuracy of the predictions is decreased.

The present model has been validated against uniaxial tension tests at different temperature and strain rates and pressurized cylinder tests at different temperatures.

Three important issues should be noted. First, LLDPE is not a thermorheologically simple solid as it has been demonstrated by analyzing DMA test results. LLDPE is semi-crystalline, as it includes both amorphous and crystal phases. For thermorheologically complex materials the time-temperature principle breaks down and the temperature shift factors depend on frequency. In the development of the present model, the same temperature shifts were applied to all creep compliance components obtained directly from creep tests and this approximation worked well with the creep master curves. For dynamic loading at high frequencies the material behavior can be expected to deviate from the creep tests, hence the master curves may not be applied to such loading cases. Second, the out-of-plane thermoviscoelastic properties were obtained by calibrating the model parameters with the measured nonlinear behavior of different kinds of test samples. It is not known if the optimization problem from which the model parameters were obtained is mathematically well posed. This is a topic for further investigation. Third, the predicted out-of-plane behavior of StratoFilm has been shown to be strongly dependent on the particular value chosen for the out-of-plane CTE, although the in-plane behavior is rather insensitive. It would be interesting to carry out direct out-of-plane measurements of StratoFilm to understand its behavior more fully.

Acknowledgements We thank Drs. Wolfgang Knauss (California Institute of Technology), James Rand (Winzen Engineering), and David Wakefield (Tensys Limited) for helpful comments and discussions. We thank Dr He of NASA GSFC for providing DMA test data on StratoFilm, Dr W.N. Warner of NASA Jet Propulsion Laboratory for assistance in measuring the out-of-plane CTE of StratoFilm, and Dr L. Young of NASA Wallops for providing test data. This research was supported by the NASA Balloon Program Office. Financial support from the Croucher Foundation (Hong Kong) for Kawai Kwok is also gratefully acknowledged.

References

1. Smith, I.M., 2004. The NASA balloon program: Looking to the future. Advances in Space Research 33, 1588–1593.

2. Smith, I.M., Rainwater, E., 2004. Optimum designs for superpressure balloons. Advances in Space Research 33, 1688–1693.
3. Schapery, R.A., 1966. An engineering theory of nonlinear viscoelasticity with applications. International Journal of Solids and Structures 2, 407–425.
4. Schapery, R.A., 1969. On the characterization of nonlinear viscoelastic materials. Polymer Engineering and Science 9, 295–310.
5. Schapery, R., 1997. Nonlinear viscoelastic and viscoplastic constitutive equations based on thermodynamics. Mechanics of Time-Dependent Materials 1, 209–240.
6. Boyce, M.C., Parks, D.M., Argon, A.S., 1988. Large inelastic deformation of glassy polymers. Part I: Rate dependent constitutive model. Mech. Mater. 7, 15–33.
7. Bergstrom, J.S., Boyce, M.C., 1998. Constitutive modeling of the large strain time-dependent behavior of elastomers. Journal of the Mechanics and Physics of Solids 46 (5), 931–954.
8. Dupaix, Rebecca B., Boyce, Mary C., 2006. Constitutive modeling of the finite strain behavior of amorphous polymers in and above the glass transition. Mech. Mater. 39, 39–52.
9. Caruthers, J.M., Adolf, D.B., Chambers, R.S., Shrikhande, P.,2004. A thermodynamically consistent, nonlinear viscoelastic approach for modeling glassy polymers. Polymer 45, 4577–4597.
10. Wineman, A., 2009. Nonlinear viscoelastic solids a review. Math. Mech. Solids 14, 300–366.
11. Rand, J., Henderson, J., Grant, D., 1996. Nonlinear behavior of linear low-density polyethylene. Polymer Engineering and Science 36, 1058–1064.
12. Rand, J., Sterling, W., 2006. A constitutive equation for stratospheric balloon materials. Advances in Space Research 37, 2087–2091.
13. Rand, J., Wakefield, D., 2010. Studies of thin film nonlinear viscoelasticity for superpressure balloons. Advances in Space Research 45, 56–60.
14. Gerngross, T., Xu, Y., Pellegrino, S., 2008. Viscoelastic behavior of pumpkin balloons. Advances in Space Research 42, 1683–1690.
15. Knauss, W., Emri, I., 1981. Nonlinear viscoelasticity based on free volume consideration. Computers and Structures 13, 123–128.
16. Kwok, K., Pellegrino, S., 2011. Large strain viscoelastic model for balloon film. In: 11th AIAA Balloon Systems Conference. Virginia Beach, VA.
17. Lakes, R. S., 1999. Viscoelastic Solids. Boca Raton, CRC Press.
18. Brinson, H. F. and L. C. Brinson (2008). Polymer Engineering Science and Viscoelasticity: An Introduction. New York, Springer
19. Knauss, W., Emri, I., 1987. Volume change and the nonlinearly thermo-viscoelastic constitution of polymers. Polymer Engineering and Science 27, 86–100.
20. Losi, G., Knauss, W., 1992. Free volume theory and nonlinear thermoviscoelasticity. Polymer Engineering and Science 32, 542–557.
21. Doolittle, A., 1951. Studies in newtonian flow. ii the dependence of the viscosity of liquids on free-space. Journal of Applied Mechanics 22, 1471–1475.
22. Popelar, C., Liechti, K., 1997. Multiaxial nonlinear viscoelastic characterization and modeling of a structural adhesive. Journal of Materials and Technology 119, 205–210.
23. Popelar, C., Liechti, K., 2003. A distortion-modified free volume theory for nonlinear viscoelastic behavior. Mechanics of Time-Dependent Materials 7, 89–141.
24. Schwarzl, F.R., Struik, L.C.E., 1968. Analysis of relaxation measurements. Advances in Molecular Relaxation Processes, 1 (3), 201-255, 1968.
25. Capodagli, J., Lakes, R., 2008. Isothermal viscoelastic properties of pmma and ldpe over 11 decades of frequency and time: a test of time-temperature superposition. Rheologica Acta 47, 777–786.
26. Caruthers, J. M., Cohen, R. E., 1980. Consequences of thermorheological complexity in viscoelastic materials. Rheologica Acta 19, 606–613.
27. Young, L., 2010. CTE curve fitting data. NASA Balloon Program Office report.
28. Vic-3D 2010, Correlated Solutions Inc.
29. Sutton, M. A., Orteu, J. J., Schreier, H. W., 2009. Image correlation for shape, motion and deformation measurements: basic concepts, theory and applications. Springer.
30. Williams, M., Landel, R., Ferry, J., 1955. The temperature dependence of relaxation mechanisms of amorphous polymers and other glass-forming liquids. Journal of the American Chemical Society 77, 3701–3707.
31. Park, S. W., Kim, Y. R., 2001. Fitting Prony-series viscoelastic models with power-law presmoothing. ASCE Journal of Materials in Civil Engineering 13, 26–32.
32. Schapery, R. A., 1974. Viscoelastic behavior and analysis of composite materials. Mechanics of Composite Materials.(A 75-24868 10-39) New York, Academic Press, Inc., 1974, 85-168.

33. Lai, J., Bakker, A., 1996. 3-d Schapery representation for nonlinear viscoelasticity and finite element implementation. Computational Mechanics 18, 182–191.
34. Hansen, N., Müller, S.D., Koumoutsakos, P., 2003. Reducing the Time Complexity of the Derandomized Evolution Strategy with Covariance Matrix Adaptation (CMA-ES). Evolutionary Computation 11, 1-18.
35. Hansen, N., 2012. The CMA Evolutionary Strategy. Downloaded from https://www.lri.fr/ hansen/cmaesintro.html on December 12, 2012.